Design Aspects of Double-Sided Rotor Radial Flux Air-Cored Permanent-Magnet Wind Generator

Johannes Abraham Stegmann and Maarten J. Kamper, *Senior Member, IEEE*

***Abstract*—The electromagnetic and mechanical design aspects of optimally designed double rotor radial flux permanent-magnet wind generators with nonoverlap air-cored (ironless) stator windings are analyzed in this paper. An accurate analytical design optimization method is proposed. The analytical model is confirmed by finite-element analysis. It is shown, among other things, that the electromagnetic design, and not the mechanical design, determines the rotor yoke dimensions and, thus largely, the mass and cost of the generator.**

***Index Terms*—Air cored, design, double rotor, finite element (FE), permanent magnet (PM), radial flux, wind generator.**

NOMENCLATURE

a	Number of parallel circuits.
B_g	Peak air-gap flux density (in teslas).
B_r	Residual magnetic flux density (in teslas).
B_1	Peak of fundamental air-gap flux density (in teslas).
d	Average stator diameter (in meters).
d_c	Diameter of stranded conductor (in meters).
g	Air-gap length between stator and magnet (in meters).
h	Height (thickness) of stator winding (h), magnet (h_m), and yoke (h_y) (in meters).
H_c	Coercive magnet field strength (in ampere per meter).
J	RMS current density (in ampere per meter square).
k_f	Copper filling factor.
k_w	Winding factor.
k_e	End-winding constant.
κ	Per unit coil-side width.
ℓ	Axial active length (in meters).
M	Mass of copper (M_{cu}), magnet (M_m), yoke (M_y), and total (M_t) active mass (in kilograms).
N	Number of turns per coil.
n_c	Number of parallel stranded conductors.
η	Machine efficiency $[1-(P_{cu}+P_e)/P_d]$.
P_{cu}	Stator copper losses (in watts).
P_d	Developed power (in watts).
P_e	Eddy-current losses in stator coils (in watts).
p	Number of permanent-magnet poles.
Q	Number of stator coils.
r_c	Radius of curvature.
T_d	Developed torque (in newton meters).
σ	Density of copper (σ_{cu}), magnet (σ_m), and iron (σ_{fe}) (in kilograms per cubic meter).
γ	Yield stress of mild steel $= 250 \times 10^6$ Pa.
ρ_t	Resistivity of copper (in ohmmeter).
θ	Current phase angle (in radians).
ω	Electrical frequency $= 2\pi f$ (in radians per second).
ω_r	Turbine rotor speed (in radians per second).
τ_m	Per unit magnet pitch.
μ_o	Permeability of air $= 4\pi \times 10^{-7}$ H $\cdot$ m^{-1}.

I. INTRODUCTION

THE USE of double rotor air-cored winding permanent-magnet (PM) machines has numerous advantages such as no core losses, zero cogging torque, no attraction forces between the stator and the rotor, and possibility of *in situ* replacement of faulty stators. The use of nonoverlapping concentrated stator windings has been shown to be very advantageous in terms of ease of manufacturing and assembling and in saving copper and the performance of the machine [1], [2]. However, the drawbacks of these machines, namely, the large attraction forces between PM rotors and the relatively large amount of PM material used due to the large air gap, seem to be overwhelming. The latter is possibly the reason for the relatively little work that has been published on these machines and the low number of applications at larger power levels [3]–[10].

No work, as far as the authors know, has been published on the optimal design and critical evaluation of radial flux PM (RFPM) air-cored machines and to what extent these machines have the same drawbacks as their axial flux PM (AFPM) counterparts. Thus, in this paper, consideration is given to the electromagnetic and mechanical design of the double rotor RFPM air-cored generator through analytical and finite-element (FE) analysis. The aim of the optimal design is to minimize the active mass of the generator subject to power and efficiency constraints. Mass and cost explanations are, thus, of interest. The focus of this paper is on small-scale (sub-100 kW) direct drive wind generator applications.

Manuscript received April 7, 2010; revised July 23, 2010; accepted October 10, 2010. Date of publication January 6, 2011; date of current version March 18, 2011. Paper 2010-EMC-133.R1, presented at the 2009 IEEE Energy Conversion Congress and Exposition, San Jose, CA, September 20–24, and approved for publication in the IEEE TRANSACTIONS ON INDUSTRY APPLICATIONS by the Electric Machines Committee of the IEEE Industry Applications Society.

The authors are with the Department of Electrical and Electronic Engineering, Stellenbosch University, Stellenbosch, Matieland 7602, South Africa (e-mail: abris@sun.ac.za; kamper@sun.ac.za).

Color versions of one or more of the figures in this paper are available online at http://ieeexplore.ieee.org.

Digital Object Identifier 10.1109/TIA.2010.2103541

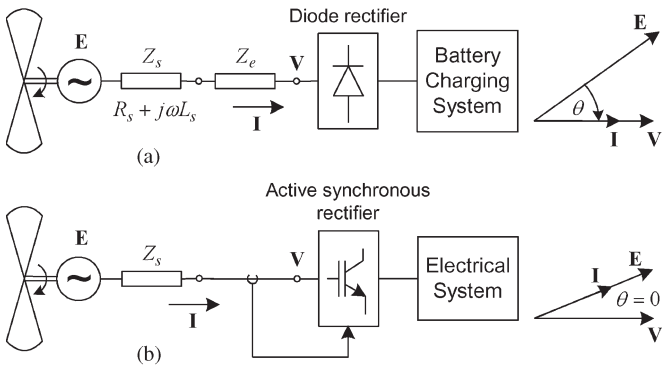

Fig. 1. Single-line diagrams of PM wind generators connected to different front-end rectifiers.

II. Wind Generator Systems

Small-scale PM wind generators can be connected to a battery-charging system via an uncontrolled diode rectifier, as shown in Fig. 1(a). These generators can also be connected to battery-charging or inverter-fed grid-connected systems via an active synchronous rectifier, as shown in Fig. 1(b).

In the case of an uncontrolled diode rectifier, the fundamental component of the generator current is in-phase with the terminal voltage, as shown in the phasor diagram in Fig. 1(a). The current angle θ, in this case, is equal to the phase angle between the induced voltage $\mathbf{E}$ of the generator and the voltage $\mathbf{V}$ at the diode bridge. To ensure sinusoidal currents and also an improved power matching with the turbine, an external reactance X_e (inductive or capacitive) [8], [11] may be used in series with the impedance $Z_s = R_s + j\omega L_s$ of the generator and connecting cable. This reactance has a direct effect on the current angle of the system.

In the case of an active synchronous rectifier, the phase currents are controlled to be sinusoidal to ensure high torque quality and low noise coming from the generator. The currents are also controlled to be in-phase with the induced voltage $\mathbf{E}$ to ensure the maximum torque per copper loss operation of the generator. The current angle in this case becomes zero, as shown in Fig. 1.

In the design and in the design optimization of the generator, it is, thus, important to take into account the type of load system that the generator is connecting to. In cases where the current angle is not zero ($\theta \neq 0$), the generator does not operate at its optimum performance. The implication of this is that an oversized machine must be designed to generate the necessary torque and power and to generate this torque and power at a satisfying efficiency.

III. Mathematical Model

A cross section with the dimensional parameters of the double rotor RFPM machine is shown in Fig. 2. For this machine, a nonoverlap (nonoverhang) stator winding is compulsory; otherwise, the assembling of the stator will not be possible or will be very difficult. A little space for the end windings inside the machine makes this an even more important winding topology.

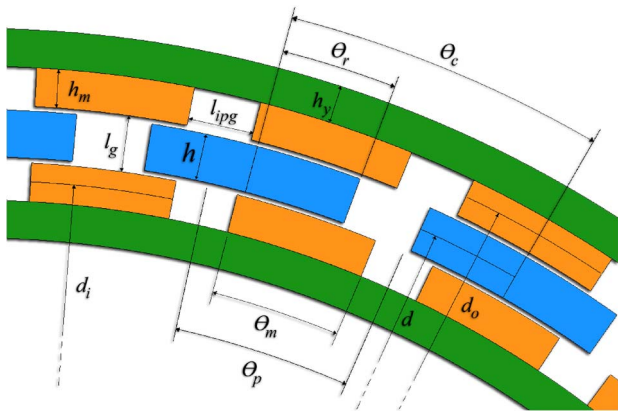

Fig. 2. Cross section of the double rotor air-cored RFPM generator.

The required performance of the RFPM generator and the dimensional parameters that have to be optimized in the design are defined, respectively, in matrix format by $\mathbf{U}$ and $\mathbf{X}$ as

$$\mathbf{U} = \begin{bmatrix} P_d \\ \omega_r \\ \eta \end{bmatrix} \quad \mathbf{X} = \begin{bmatrix} d \\ \ell \\ h \\ h_m \\ h_y \end{bmatrix}. \tag{1}$$

Two important required performance parameters of the generator that are functions of $\mathbf{X}$, namely, the developed torque $T_d(\mathbf{X})$ and the copper losses $P_{cu}(\mathbf{X})$, can be determined from the known required performance given in (1) as

$$\mathbf{G} = \begin{bmatrix} T_d(\mathbf{X}) \\ P_{cu}(\mathbf{X}) \end{bmatrix} = \begin{bmatrix} 1/\omega_r \\ k(1-\eta) \end{bmatrix} P_d \tag{2}$$

where $k < 1$ gives the ratio of the copper losses to the total losses of the machine. As the air-cored stator winding RFPM machine has practically no iron losses and if the mechanical wind and friction losses are ignored in the design optimization, the only remaining losses in the machine are the copper losses P_{cu} and the eddy current losses in the stator winding P_e. Hence, k of (2) is given by

$$k = \frac{P_{cu}}{P_{cu} + P_e}. \tag{3}$$

The eddy current losses in the air-cored stator winding PM machines can be calculated from [12] as

$$P_e = 1.7NQn_c \left(\frac{\pi \ell d_c^4 B_1^2 \omega^2}{16\rho_t} \right) \tag{4}$$

where the factor 1.7 accounts for the eddy current losses due to all of the air-gap flux density harmonics. The eddy current losses can be made substantially small by using parallel connected coils and parallel stranded wires to reduce the conductor diameter d_c in (4), as described by [12]. Hence, k can be taken in the design in (2) as between $2/3 < k < 1$, and a typical value to start with is $k = 0.7$. If this value makes it difficult to apply it in practice, then k can be adjusted, and the machine can be quickly reoptimized in its design. Note that including the eddy current losses as part of the design optimization makes the design optimization unnecessarily difficult.

A. Torque

As derived in [1], [2], and [9] for linear, axial, and radial flux air-cored stator PM machines, the developed torque of the generator can be expressed by

$$T_d = k_w C_1 K_1 \tag{5}$$

where k_w is the stator winding factor given in the Appendix, C_1 is a function of the copper losses and is given by

$$C_1 = B_1 \sqrt{\frac{\pi P_{cu} \kappa k_f}{2\rho_t}} \cos\theta \tag{6}$$

and K_1 is a machine constant as a function of d, ℓ, and h of (1) as

$$K_1 = \sqrt{\frac{h\ell d^3}{2(1 + k_e d/\ell)}} \tag{7}$$

where k_e is an end-winding constant derived in the Appendix. The important coil width factor κ used in, among others, (6) is defined in Fig. 2 as

$$\kappa = \frac{\theta_r}{\theta_c} \tag{8}$$

and is assigned with a constant value in the design, as explained in the Appendix. The current angle θ of (6) depends on the system (Fig. 1) where the generator is connected.

It is important to point out that the constant K_1 of (7) can be calculated from the known (required) torque of (2) and from (5) and (6) as

$$K_1 = \frac{T_d}{k_w C_1}. \tag{9}$$

B. Copper Losses

The copper losses in the stator winding in Fig. 2 can be expressed as

$$P_{cu} = C_2 K_2 \tag{10}$$

where C_2 is another machine constant given by

$$C_2 = 2\pi \kappa k_f \rho_t J^2 \tag{11}$$

and K_2 is a constant, but it is also a function of d, ℓ, and h as

$$K_2 = h\ell d(1 + k_e d/\ell). \tag{12}$$

The current density J of (11) must be selected in the design. The selection of J plays an important role in the outcome of the design, as shown in the next section.

Similar to (9), K_2 can be calculated from the known (calculated) copper losses of (2) and from (10) and (11) as

$$K_2 = \frac{P_{cu}}{C_2}. \tag{13}$$

C. Stator Length and Diameter Relationship

A relation between the axial length ℓ and diameter d of the stator winding can be derived from (7) and (12) by taking

$$\frac{\sqrt{K_2}}{K_1} = \sqrt{2}\left(\frac{1}{d} + \frac{k_e}{\ell}\right). \tag{14}$$

From (14), it follows that

$$\ell = \frac{k_e}{K_3 - 1/d} \quad \left\{ K_3 = \frac{\sqrt{K_2/2}}{K_1} \right\}. \tag{15}$$

According to (15), there exists a functional relationship between ℓ and d of the stator winding, which is independent from h. Hence, if d is chosen, then ℓ can be determined from (15). With ℓ and d known, h can be determined from (12). In this way, three of the important dimensional parameters of (1) can be determined, which satisfy the required performance $\mathbf{U}$ and $\mathbf{G}$ of (1) and (2) of the generator.

D. Magnet and Yoke Heights

The remaining dimensional parameters that have to be determined in the design according to (1) are the magnet height h_m and the yoke height h_y of the generator. These heights must be designed in such a way that the required flux density in the air gap is obtained. A flat-topped trapezoidal shaped air-gap flux density waveform is shown in the Appendix to be a good approximation of the real air-gap flux density. The ratio of the flat-topped flux density value B_g to the peak fundamental component B_1 is determined from the FE analysis (Appendix) for a per unit magnet pitch of $\tau_m = 0.7$ as

$$b = \frac{B_g}{B_1} \approx 0.937 \quad [\tau_m = 0.7] \tag{16}$$

where τ_m is defined in Fig. 2 as

$$\tau_m = \frac{\theta_m}{\theta_p}. \tag{17}$$

τ_m plays an important role, among other things, in the leakage flux constraints discussed in Section III-F. An optimal τ_m value found by [6] that can be used in the analytical design is $\tau_m = 0.7$. Note that, after the first analytical design optimization of the machine, the b value in (16) can be updated from one static FE air-gap field solution of the first designed machine, then followed by a quick second analytical design optimization to confirm or improve the optimum design results.

The electromagnetic design of the magnet and yoke heights depends on the permeability and BH characteristics of the magnet and yoke material. Due to the relatively large air gap of the air-cored stator RFPM machine, a high-energy product rare-earth magnet material must be used for the PMs. For the solid rotor yokes, a mild steel material is used. The BH characteristics of the NdFeB magnet material (grade N48) and mild steel are shown in Fig. 3. Due to the large air gap, the rotor yokes can be put fairly deep into saturation before they start to substantially increase the magnetic circuit reluctance. By choosing a fixed value for the yoke flux density B_y, the

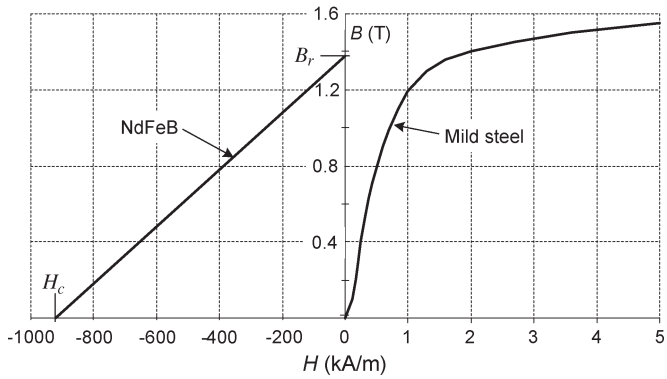

Fig. 3. BH characteristics of the NdFeB (N48) and mild steel material.

magnetic field strength in the yoke H_y can be determined from the mild steel BH curve, as shown in Fig. 3. Typical values are $B_y = 1.5$ T and $H_y = 4000$ At/m.

Consider a PM pole that generates an MMF of $F_g = I_m = H_c h_m$ across the magnetic circuit. Then, the MMF equation for the magnetic circuit can be written as

$$H_c h_m = H_m h_m + H_g \ell_g/2 + H_y \ell_y \tag{18}$$

where ℓ_g and ℓ_y are the lengths defined in Fig. 2 and given by

$$\begin{aligned} \ell_g &= h + 2g \\ \ell_y &= \frac{\pi d}{2p}. \end{aligned} \tag{19}$$

In Fig. 3, the permeability of the magnet material can be determined as $\mu_m = B_r/H_c$. From this and by taking the flux density in the magnet as the same as in the air gap, (18) can be expressed as

$$H_c h_m = B_g \left(\frac{H_c}{B_r}\right) h_m + \left(\frac{B_g}{\mu_0}\right) \frac{\ell_g}{2} + H_y \ell_y. \tag{20}$$

By rearranging (20), the magnet height can be calculated as

$$h_m = \frac{B_g \ell_g + 2\mu_0 H_y \ell_y}{2\mu_0 H_c [1 - B_g/B_r]}. \tag{21}$$

As the half of the flux per magnet pole is set up in the back iron yoke, the yoke height can simply be calculated from the ratio of the air-gap and yoke flux densities as

$$h_y = \frac{\pi d \tau_m}{2p} \left(\frac{B_g}{B_y}\right). \tag{22}$$

Note from the Appendix that the curvature has a minimal effect on the difference in the air-gap flux densities at the inner and outer layers of the stator winding and on the difference in the MMF drops in the inner and outer iron yokes. The curvature effect, thus, is as a good approximation ignored in the design equations earlier.

E. Active Mass

With $\mathbf{X}$ of (1) calculated, the active mass of the double rotor air-cored stator RFPM machine can be determined. This mass consists of the mass of the PMs, stator copper, and rotor yokes. The mass of the PM and rotor yoke materials is, respectively, given by

$$M_m = 2\pi \sigma_m \tau_m h_m \ell d \tag{23}$$

$$M_y = 2\pi \sigma_{fe} h_y \ell d. \tag{24}$$

The stator copper mass can be determined as

$$\begin{aligned} M_{cu} &= 2\pi \sigma_{cu} \kappa k_f h \ell d (1 + k_e d/\ell) \\ &= 2\pi \sigma_{cu} \kappa k_f K_2. \end{aligned} \tag{25}$$

Substituting (13) and (11) into (25) results in an equation for the copper mass as

$$M_{cu} = \frac{P_{cu} \sigma_{cu}}{\rho_t J^2}. \tag{26}$$

This is an interesting result as the copper mass is independent from $\mathbf{X}$ of (1). It is, thus, not necessary to consider the copper mass in the design optimization of $\mathbf{X}$ as it is a constant. However, the determined P_{cu} and the chosen J in (26) are important parameters in the final outcome of the generator design.

F. Leakage Flux Constraints

Due to the relatively large air gap of the air-cored stator PM machine, a high amount of leakage flux can easily be set up between adjacent magnets tangentially in the air gap. The tangential leakage flux in the air gap must be minimized as it is detrimental to the performance of the machine [12]. Furthermore, flux can also leak from the magnet pole edges directly back to the iron yoke. To ensure a minimum leakage flux or to ensure a strong radial flux between opposite poles, the design of the machine is subjected to the following constraints, as explained in the Appendix:

$$\begin{aligned} h_m &> \frac{1}{2} \ell_g \\ \ell_{ipg} &= \frac{\pi d_i}{p} (1 - \tau_m) > \ell_g \end{aligned} \tag{27}$$

where d_i and ℓ_{ip} are defined in Fig. 2. These two constraints often make designs invalid; in this case, d and/or p must be altered.

IV. Design Optimization

The mathematical model and constraints of the previous section are used in a case study to optimize the design of a 4-kW air-cored RFPM wind generator. The generator is used in a direct battery-charging system.

A. Site- and Turbine-Specific Design

When optimizing the design of a wind turbine and a wind generator, site-specific characteristics can be included in the design process. Site-specific designs are advantageous in scenarios where a large number of units are installed in one location, e.g., an offshore wind farm.

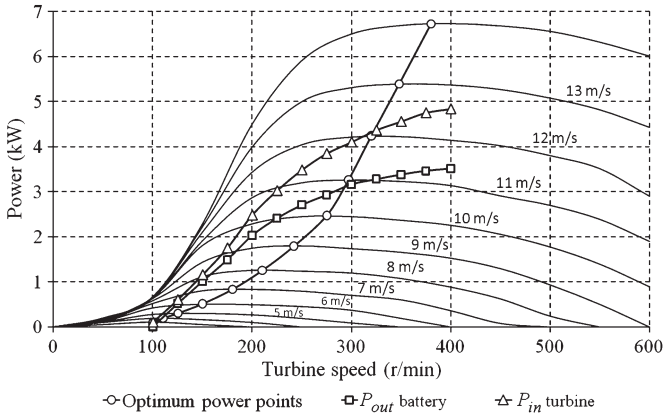

Fig. 4. Turbine power versus speed curves (3.6-m blade diameter) and measured system power with battery-charging load.

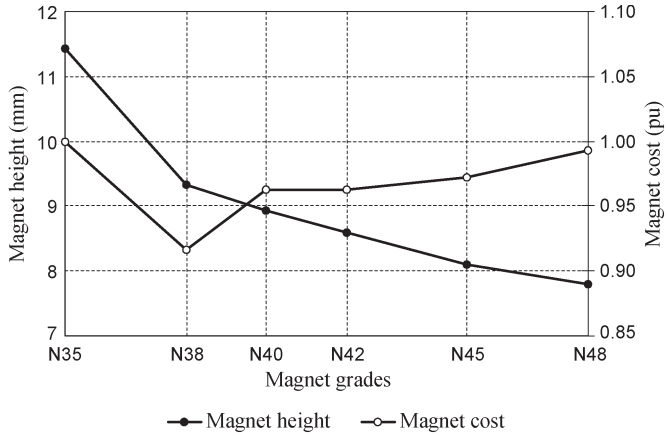

Fig. 5. Magnet cost and magnet height versus magnet grade for a given air-gap flux density (cost data obtained in May 2009).

TABLE I
CONSTANT PARAMETERS

$\rho_t = 2.1 \times 10^{-8}\,\Omega$m	$\kappa = 0.37$	$B_r = 1.38$ T	$g = 1.5$ mm
$\sigma_{fe} = 7800$ kg/m^3	$k_f = 0.42$	$H_c = 923$ kA/m	$\tau_m = 0.7$
$\sigma_{cu} = 8100$ kg/m^3	$k_w = 0.875$	$B_y = 1.55$ T	$\cos(\theta) = 0.629^*$
$p = 24, 28, 32, 36, 40$	$B_1 = 0.774$ T	$H_y = 5000$ A/m	$J \leq 5$ A/mm^2

* with $p = 32$ and 300 r/min

The industry trend, however, is rather to produce a standard range of turbine-generator systems than to redesign the system for each new site [13]. It must also be mentioned that the rated electrical power of the turbine-generator systems is defined typically at wind speeds between 14 and 16 m/s [13], although in lower wind speed regions and countries, this can be at wind speeds between 10 and 12 m/s.

In this paper, the wind generator is designed according to the power curves of a given and available wind turbine (thus turbine specific). From these power curves, at a selected wind speed of 12 m/s, the rated electrical power of the turbine-generator is defined.

B. Wind Generator System and Specifications

The air-cored RFPM wind generator is designed to operate in a battery-charging system, as shown in Fig. 1(a). The dc output of the diode rectifier in this case is connected directly to the battery bank to keep the system as simple and cheap as possible. The batteries are protected against overcharging by dissipating the excess energy into a parallel connected resistor bank.

Connecting an air-cored generator with its low internal inductance directly to a diode rectifier causes the generator current to become nonsinusoidal and the generator to be very noisy. Also, a good turbine power matching is only obtained at a small range of wind speeds. To solve these two problems, a three-phase external inductor L_e is used in series with the diode rectifier to act as an additional series reactance $Z_e = jX_e = j\omega L_e$, as shown in Fig. 1(a). This solution has been proposed and analyzed in detail in [8]. However, the use of an additional series inductance comes at the expense of a large current angle θ, as shown in Fig. 1(a), and an oversized generator.

The power versus speed curves of the wind turbine considered are shown in Fig. 4. The turbine-generator's rated operating point is chosen to be at 12 m/s and 300 r/min of turbine speed, which gives a rated turbine-generator power of 4.2 kW. The cut-in operating point is chosen at 3 m/s of wind speed and 100 r/min of turbine speed. The efficiency of the relatively small direct drive generator is chosen to be not less than 90%, but a higher efficiency is also not chosen as it considerably increases the size of the generator, which is already operating at a large (poor) current angle. The required generator performance $\mathbf{U}$ of (1) is thus given by

$$\mathbf{U} = \begin{bmatrix} P_d \\ \omega_r \\ \eta \end{bmatrix} = \begin{bmatrix} 4200 \\ 31.42 \\ 0.9 \end{bmatrix}. \tag{28}$$

From (28) and (2), it follows that

$$\mathbf{G} = \begin{bmatrix} T_d \\ P_{cu} \end{bmatrix} = \begin{bmatrix} 134 \\ 316 \end{bmatrix} \tag{29}$$

with k of (2) and (3) taken as $k = 0.75$.

C. Magnet Grade

The question in relation to magnet mass and strength is if a low- or high-grade material must be used for the air-cored stator PM machines. To investigate this, a study was conducted through FE analysis to determine the magnet cost and magnet mass versus magnet grade for a given air-gap flux density. This led to the surprising result shown in Fig. 5 for the NdFeB magnets. The graph illustrates a large reduction in magnet height (and thus magnet and generator mass) versus magnet grade, with only a marginal increase in magnet cost. The consequence of this is that the strongest magnet grade must be chosen in the design of the machine. Thus, in this case, the N48 magnet grade was used.

D. Constant Parameters

A list of the constant parameters used in the design optimization of the air-cored RFPM generator is given in Table I. The current density is varied manually in the design optimization as

a parameter to get the best result. However, only designs where $J < 5$ A/mm^2 are accepted.

To ensure an average air-gap flux density of 0.7 T, the flux density in the design is taken a fraction higher, namely, $B_g = 0.725$ T, which results in $B_1 = 0.774$ T according to (16). For the PMs, NdFeB magnets that are grade N48 are chosen based on the outcome of Section IV-C. As given in Table I, different pole numbers are used in the design optimization of the generator to determine the best choice.

In Fig. 1(a), $L_e \gg L_s$ so that L_e could be determined beforehand as $L_e = 1.5$ mH according to the chosen cut-in and rated operating points of the turbine-generator system [8]. From this, the current angle for the wind generator system at 80 Hz, with $p = 32$, is determined approximately as $\theta = 51°$, which results in $\cos(\theta) = 0.629$, as given in Table I and as used in (6).

The winding analysis in [1], as also explained in the Appendix, shows that the per unit coil-side width of (8) can be taken in the design as $\kappa = 0.37$. The fill factor $k_f = 0.42$ for the wound stator coils is obtained from practical experience. Finally, the temperature of the stator winding is taken as fairly high, namely, 80 °C, which results in the resistivity as given in Table I.

E. Design Optimization

In the design optimization, the mass of the active material of the generator is minimized. The effect that this minimization has on the construction mass of the generator is not considered in this paper. It is, however, important to consider the construction mass, specifically for large wind generators.

Hence, the objective function $F(\mathbf{X})$ that has to be minimized in the design optimization subject to the performance constraints of (28) and (29) and the leakage flux constraints of (27) can be expressed as

$$F(\mathbf{X}) = w_1 M_m(\mathbf{X}) + w_2 M_y(\mathbf{X}) \tag{30}$$

where w_1 and w_2 are the weighting factors and $\mathbf{X}$ is given by (1). Note that M_{cu} is not included in (30) as it is a constant according to (26). M_{cu}, however, must be included in the total active mass when comparing optimum designed generators with different pole numbers. In the case where $w_1 = w_2$ in (30), then the total active mass of the generator is, in effect, minimized in the optimization.

The first step in the design optimization is to calculate the constants K_1, K_2, and K_3 according to (9), (13), and (15), respectively. The next step is to vary the diameter d and to calculate a unique value for ℓ for each d from (15), and then, calculate unique values for h, h_m, and h_y by (12), (20), and (21), respectively. From this, M_m and M_y are calculated, respectively, by (23) and (24), and finally, $F(\mathbf{X})$ is calculated by (30). The d value is changed in steps from an initial value until the minimum of the function is obtained. At each d value, the leakage flux constraints of (27) are checked, and if one or both of these constraints are not satisfied, then that design is marked as invalid. The whole design optimization can be implemented in a simple spreadsheet program.

The different pole numbers given in Table I have been investigated in the design optimization. For each pole number, the current density has been varied to get an optimum and valid design. The outcome of this investigation clearly shows that, the higher the pole number is, the lower is the active mass. However, high pole number designs tend to have large diameters, which might become impractical and/or which might increase the construction mass of the generator. Also, with higher pole numbers, the generator supply frequency is higher, which, among other things, means that more effort must be taken to keep the eddy current losses within limits. From this investigation, a pole number of $p = 32$ has been chosen for the air-cored stator RFPM generator.

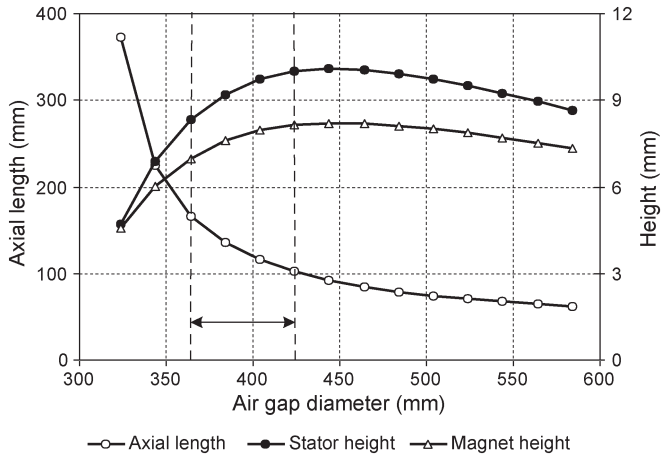

Fig. 6. Length and height versus diameter of the air-cored RFPM generator.

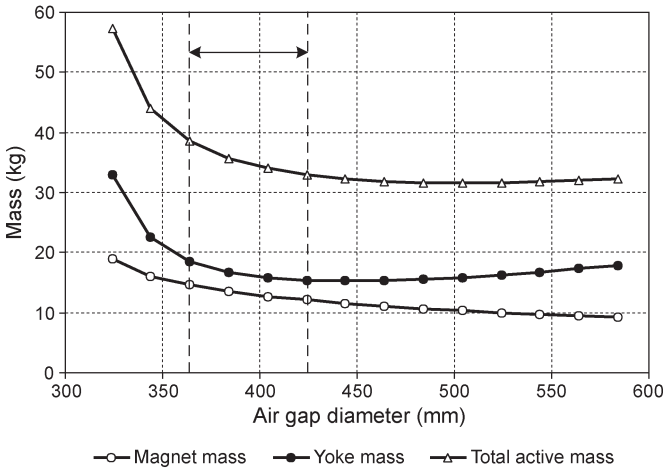

Fig. 7. Mass versus diameter of the air-cored RFPM generator.

The variations of the dimensional and mass parameters of a 32-pole wind generator with machine diameter d are shown in Figs. 6 and 7. First, it is shown that, for diameters between $364 \leq d \leq 424$ mm, the designs are invalid as (27) is not satisfied. Second, it is shown in Fig. 7 that, if the magnet mass is minimized at all costs, i.e., with $w_1 \gg w_2$ in (30), this leads to very large machine diameters that increase the construction mass. It is rather better and more practical to minimize the total active mass of the generator $(w_1 = w_2)$. The optimum result then is at $d = 504$ mm. Due to the turbine blade dimensions, however, the generator diameter is limited to $d = 464$ mm, which, in Fig. 7, still gives a good result in terms of minimum active mass. The optimum design results of the air-cored stator

TABLE II
OPTIMUM DESIGN RESULTS

$p = 32$	$\ell = 84.9$ mm	$h_y = 7.97$ mm	$M_m = 11.06$ kg
$J = 5$ A/mm^2	$h = 10.05$ mm	$\ell/d = 0.183$	$M_y = 15.38$ kg
$d = 464$ mm	$h_m = 8.19$ mm	$M_{cu} = 5.36$ kg	$M_t = 31.8$ kg

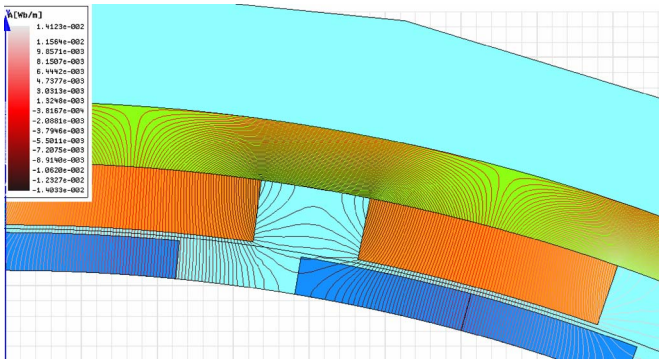

Fig. 8. Electromagnetic FE field plot of the air-cored RFPM generator.

RFPM generator at $d = 464$ mm are summarized in Table II. Note that an aspect ratio (ℓ/d) of just less than 20% and a total active mass of $M_t = 31.8$ kg are found.

V. ELECTROMAGNETIC FE ANALYSIS

Electromagnetic FE analysis has been used to confirm the analytical air-gap flux density and yoke height calculations of the optimally designed generator. The FE analysis clearly shows that the cylinder rotor yokes of the air-cored stator RFPM start to saturate magnetically if the yoke thickness becomes too thin. The magnetic flux saturation in the yokes causes a decrease of flux density in the air gap, which, in turn, negatively affects the performance of the machine.

An example of the magnetic saturation in the yoke is shown in the FE field plot in Fig. 8 of an RFPM generator that has the same dimensions as that given in Table II. The magnetic flux lines in this figure are only plotted for one-half of the machine. Clearly, magnetic saturation occurs in the steel yoke between adjacent magnet poles. To maintain an air-gap flux density of $B_g = 0.725$ T (from Section IV-D), the FE analysis shows that the yoke height must not be less than 8 mm. This corresponds very well with the analytically calculated yoke height of almost 8 mm given in Table II.

VI. MECHANICAL STRENGTH ANALYSIS

Large magnetic attraction forces on the discs of the AFPM generators have been investigated by [6] and [14] in the optimal design of such a machine. It is shown that the large attraction forces cause a large increase in mass of the PM rotor discs. In an RFPM machine, however, due to the inherent strength of the cylinder yoke topology, the thickness of the cylinder yokes can be decreased, and the machine's mass can be kept low. To calculate the minimum cylinder yoke wall thickness, the following two forces acting on the cylinder steel yokes are evident: 1) the centrifugal forces of the spinning rotor mass and 2) the magnetic attraction forces between the separate cylinder yokes.

The centrifugal force acting on a cylinder yoke can be calculated on average by

$$F_c = (M_y + M_m)\frac{d^2\omega_r^2}{8r_c} \tag{31}$$

where M_y and M_m are the total yoke and magnet mass, respectively, according to (23) and (24) and r_c is the radius of curvature [15]. From the data in Table II and at a rated speed of 300 r/min, this force is calculated as $F_c = 2.85$ kN.

The magnetic attraction force between two opposite rotor magnets, assuming the magnets to be of equal size, can be determined by

$$F_m = \frac{B_g^2}{2\mu_0}A_g \tag{32}$$

where A_g is the average area of the facing magnets. With a total of $p = 32$ magnet pairs equally spaced around the inner and outer rotors, the total intermagnet force on each rotor in the radial direction is calculated using (32) as $F = 16.22$ kN. This force is, thus, almost six times the centrifugal force acting on the cylinder yoke, as calculated earlier.

The total intermagnet force can be considered as developing an evenly distributed pressure inside the yoke, which can be used in thin-walled pressure vessel calculations (note that the FE strength analysis of the actual stress distribution shows very little difference in cylinder deformation compared to an even stress distribution). A Von Mises creation gives the minimum wall thickness of the cylinder yoke needed to withstand this force, given, on average, for the cylinders as [16]

$$h_{y(\min)} = S_f\sqrt{\frac{3}{4}}\left(\frac{dF}{2\gamma A_y}\right) \tag{33}$$

where F is the total pressure force acting on the total yoke area A_y, and S_f is a safety factor. With $S_f = 5$ and with the mild steel as the yoke material, the minimum wall thickness of the cylinder yoke is calculated from (33) as $h_{y(\min)} = 1$ mm. The tip deflection of a 1-mm-thick yoke, however, is too much. To obtain an allowable deflection, the yoke thickness is increased to 4 mm. The deflection of the tip of a 4-mm yoke is calculated as a mere 55 μm and is confirmed with the *Autodesk Inventor Pro 9* FE deformation calculator, with the result shown in Fig. 9 for the inner cylinder yoke.

The optimum yoke thickness of 4 mm from the mechanical strength analysis is half the required 8-mm yoke thickness according to the electromagnetic FE analysis in Section V. This result thus implies that mechanical considerations do not determine the optimum yoke thickness of the rotor yoke cylinders in this case.

VII. CALCULATED AND MEASURED RESULTS

A prototype of an air-cored stator RFPM wind generator has been built and tested. Some of the dimensions and machine factors of the prototype are, due to some reasons, not precisely the same as the optimum dimensions given in Table II. A

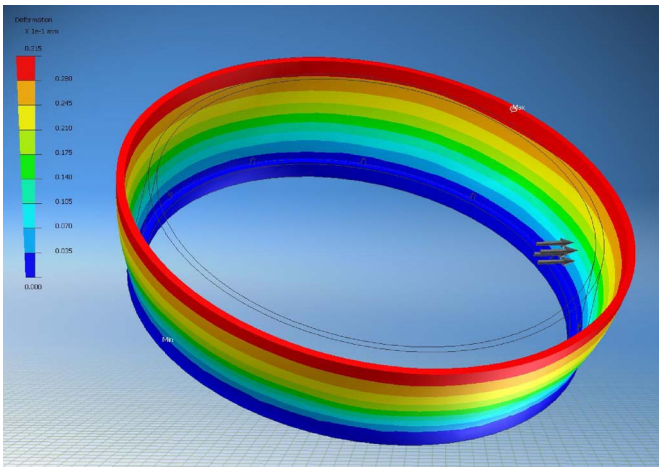

Fig. 9. Inner yoke deformation with $h_y = 4$ mm.

Fig. 10. Wind generator test setup with torque sensor.

TABLE III
DATA OF THE PROTOTYPE AIR-CORED RFPM WIND GENERATOR

$p = 32$; $Q = 24$	$a = 8$	$R_s = 52$ mΩ *	$h = 10.0$ mm
$\kappa = 0.41$	$n_c = 10$	$d = 464$ mm	$h_m = 8.2$ mm
$N = 96$	$d_c = 0.315$ mm	$\ell = 76$ mm	$h_y = 8.0$ mm

* calculated at 20 °C

photograph of the wind generator and laboratory test setup is shown in Fig. 10. In the test setup, the wind generator is connected to a variable-speed drive via a prop shaft and torque sensor. The electrical output power of the generator is measured with a power analyzer. Some of the data of the generator are given in Table III. The other data are the same as in Table I.

A. Open-Circuit Tests

The rms open-circuit-induced voltage per phase of the generator is calculated by [17] as

$$E = \frac{\sqrt{2}\omega B_1 \ell d N Q k_w}{3pa}. \tag{34}$$

The eddy current loss P_e is calculated by (4). The measured and calculated results of E and P_e versus the generator speed are shown in Fig. 11. Only the calculated results of the eddy current losses are shown as this small power loss could not be accurately measured. The close correlation between the measured and calculated results of the induced voltage is clear. The measured high-quality open-circuit sinusoidal voltages of the generator are shown in Fig. 12.

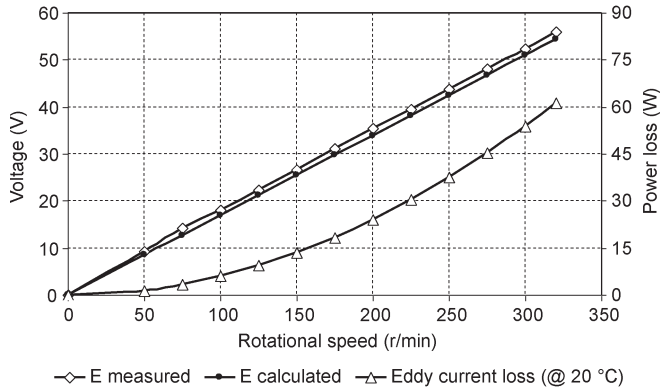

Fig. 11. Open-circuit voltage and eddy current loss versus the generator speed.

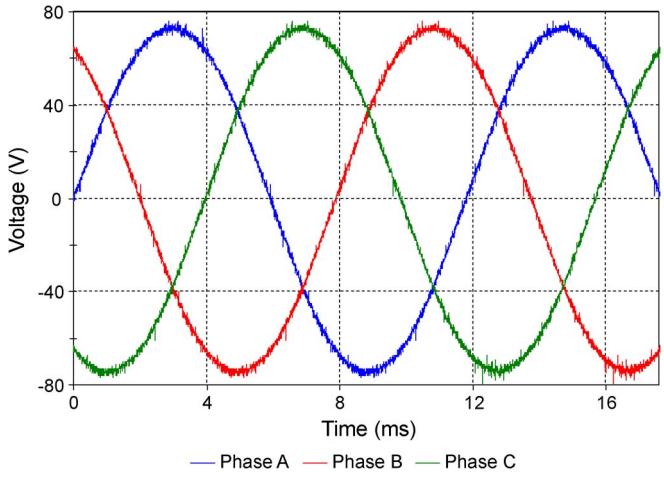

Fig. 12. Open-circuit-induced phase voltages at 320 r/min.

B. Load Tests

From accurate open- and short-circuit tests and with no transmission cable connected, the internal synchronous inductance per phase of the generator is determined as $L_s = 110$ μH. The per-phase resistance is measured at 20 °C as $R_s = 56$ mΩ, which correlates well with the calculated value in Table III.

To calculate the developed torque of the working harmonic of the generator as a function of the current, (5) is re-expressed as

$$T_d = \frac{B_1 \ell d N Q k_w}{\sqrt{2}a} I \cos(\theta) \tag{35}$$

where I is the rms phase current. For the load calculations, a per-phase equivalent circuit model is used together with (34) and (35).

Full-load tests are conducted on the generator at 320 r/min, with the generator first connected to a 36-V battery-charging load as in Fig. 1(a) and second to a three-phase resistive load

TABLE IV
MEASURED AND CALCULATED LOAD RESULTS

n_r = 320 r/min ; f = 85.3 Hz ; I = 43.8 A ; J = 5.4 A/mm^2; $P_{wf} \approx 0$ W				
L_s = 110 μH R_s = 52 mΩ	Battery charging load L_e = 1.5 mH; V_{dc} = 39.6 V		3-phase resistive load L_e = 0 mH	
Parameter ↓	Measured	Calculated	Measured	Calculated
P_d (kW)	4.4	4.3	7.3	7.1
η (%)	92	91.7	93.6	94.9
T_d (Nm)	133	129.5	219	212.6
θ (deg.)	-	52.5	-	2.73
$V_{terminal}$ (V)	51.6	51	52	52

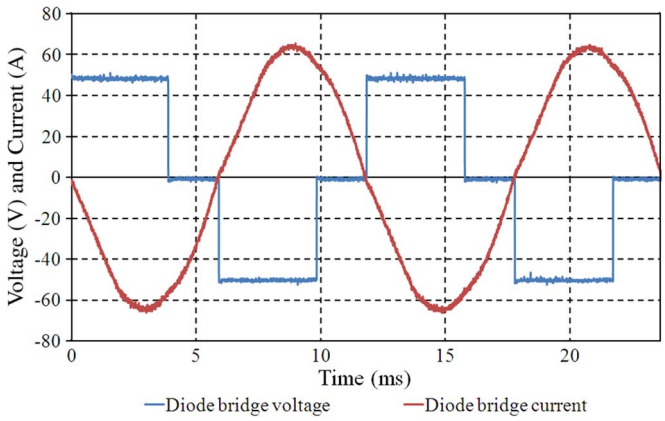

Fig. 13. Diode bridge current and voltage waveforms with the generator connected to a battery-charging load at 320 r/min.

closely equivalent to the small current angle load condition in Fig. 1(b). The calculated and measured results of these load tests are given in Table IV. In general, the calculated and measured results correlate well. Note specifically the increase in power and efficiency of the generator at small current angles. This implies that the air-cored RFPM generator must be rated at 300 r/min as 4.2 kW with a battery-charging load but as 6.7 kW with an active controlled rectifier load.

Variable-speed load tests are also conducted, with the generator connected to a 36-V battery-charging load. The measured input (turbine) and output (battery) power results of these tests are plotted on the turbine power curves, as shown in Fig. 4. It is clear that a reasonably good power matching is obtained at all wind speeds designed for. The rated current and voltage waveforms at the diode bridge of this test are shown in Fig. 13. It can be seen that the generator current is fairly sinusoidal, which results in a quiet generator operation.

Fig. 14 shows the FE transient solution of the developed torque of the generator with sinusoidal currents and with the current angle as a parameter. The good torque quality of the generator is evident. The average analytically calculated torque of (35) compares well with the FE results for the two current angles considered.

VIII. MASS OF PROTOTYPE

The total mass of the 4.2/6.7-kW prototype direct drive air-cored stator RFPM generator is determined as 59 kg by using,

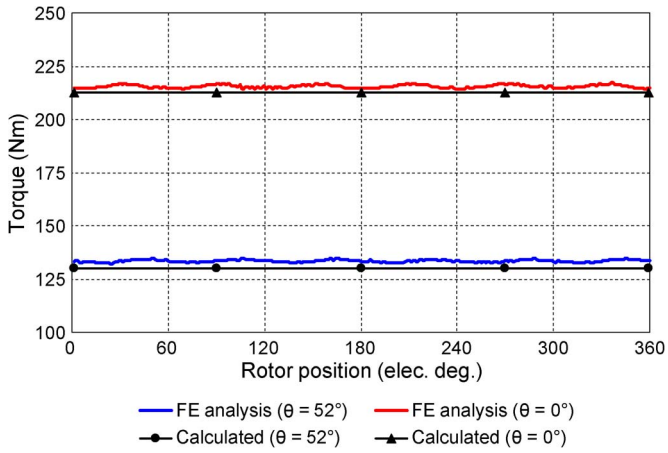

Fig. 14. Transient FE and analytically calculated developed torque with I = 43.8 A and with the current angle as a parameter.

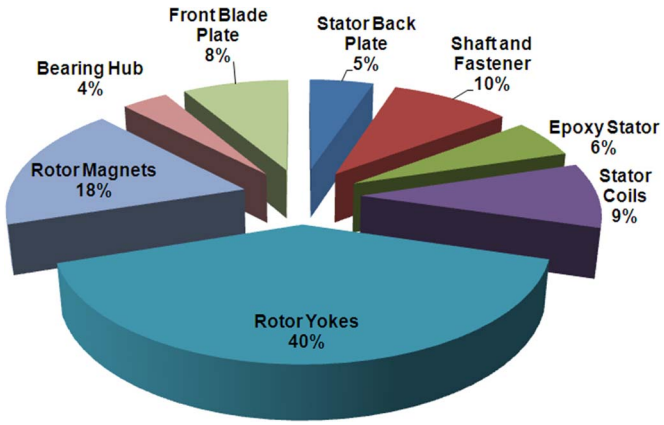

Fig. 15. Mass distribution of the prototype air-cored stator RFPM generator.

among others, the *Autodesk Inventor Pro 9* calculator. The mass distribution of all of the parts of the generator is shown in Fig. 15. It is clear that the mass of the cylinder rotor yokes dominates by far. The total active mass, including the stator epoxy, is 73% of the total mass of the generator. This shows the relatively low construction mass of this generator, which is only 27% of the total mass.

IX. CONCLUSION

An analytical calculation method has been developed whereby the electromagnetic and mechanical design of the double rotor air-cored stator RFPM machine can be optimized subject to performance constraints. The design method includes the effect of magnetic saturation. The analytical method is proved to be very accurate; thus, electromagnetic and mechanical FE analyses are not necessary per se in the design of this machine. The specific conclusions from this paper are summarized as follows.

1) The mathematical derivations show that there is a specific functional relationship between the axial length and average diameter of the machine that always satisfies the required power and efficiency of the generator. This simplifies very much the analytical design optimization of the generator.

2) If the copper losses and current density are constant in the design optimization, it is shown that the mass of copper is also a constant that is independent from the dimensions of the machine. In this regard, it is not necessary to consider the copper mass in the active mass objective function.
3) The strongest magnet grade must be used in the design of the air-cored RFPM machine as this substantially decreases the machine mass, with only a marginal increase in cost.
4) Equal priority must be given to the different active masses of the generator in the minimization of the mass objective function, rather than to give a higher priority to the magnet mass minimization.
5) The electromagnetic design, and not the mechanical design, determines the rotor yoke heights and, thus, the mass and cost of the cylinder yokes. This finding will be valid for most design cases as the finding is based on a machine with an already high pole number $(p = 32)$ and a high rated frequency (85.3 Hz). It is interesting to note that the opposite has been found for the AFPM air-cored stator machines [14].
6) The total mass of the constructed RFPM wind generator is 59 kg, which is about 36% less than the 92-kg mass of an equivalent air-cored stator AFPM wind generator. This is a significant improvement, and it shows that the relatively thin cylindrical rotors of the RFPM machine are strong enough to withstand the magnetic attraction forces.
7) It is found for the prototype air-cored stator RFPM wind generator that the construction mass amounts to only 27% of the total mass of the generator.
8) It is shown that the rated power of the air-cored stator RFPM wind generator depends on the front-end rectifier used. For the prototype wind generator, this is found to be 4.2 kW with a diode rectifier and 6.6 kW with an active synchronous rectifier, with the generator in both cases at efficiencies not lower than 90%.

The air-cored stator RFPM wind generator, together with its type of front-end rectifier used, is still to be compared with its iron-cored counterpart in terms of cost and mass. Another aspect is the high terminal short-circuit current of the air-cored generator. Under such conditions, however, the braking torque is also high so that the generator normally stops very fast. It must be noted in this regard that the air-cored stator winding is epoxy encapsulated, with a very good insulation between turns and phase coils so that internal short circuits seldom occur.

APPENDIX

A. Winding Factor k_w

The winding factor is the product of the pitch factor k_p and distribution factor k_d and is given by

$$k_w = k_p k_d. \tag{36}$$

The pitch and distribution factors of the nonoverlap air-cored windings as derived in [1] and [17] are given for the fundamental (working) harmonic by

$$k_p = \frac{\sin\left[\theta_c(1-\kappa)/2\right]\sin(\kappa\theta_c/2)}{\kappa\theta_c/2} \tag{37}$$

$$k_d = \frac{\sin\left[u(\theta_c-\pi)/2\right]}{u\sin\left[(\theta_c-\pi)/2\right]}. \tag{38}$$

In (37) and (38), θ_c is the coil span angle as defined in Fig. 2 and as given by

$$\theta_c = \frac{\pi p}{Q}. \tag{39}$$

u in (38) is the number of coils in a coil phase group, and κ in (37) is defined by (8). The studies in [1] and [2] show that the best nonoverlapping winding layouts are those layouts where $\theta_c = 4\pi/3$ and $u = 1$. Also, it is shown in [1] that the maximum torque per copper losses is obtained, where $0.37 < \kappa < 0.43$. Hence, to ensure the lowest copper mass, κ is taken in the design as $\kappa = 0.37$. If these constant values are substituted in (37) and (38), then k_w of (36) becomes $k_w = 0.875$.

B. End-Winding Constant k_e

The end-winding constant k_e in (7), (12), (14), and (25) is used in the ratio of the total end-winding length ℓ_e to the axial winding ℓ as

$$\delta_c = \frac{\ell_e}{\ell} = 2k_e\left(\frac{d}{\ell}\right). \tag{40}$$

For practical nonoverlapping windings, ℓ_e is given by [1] as

$$\ell_e = \frac{2d\theta_c}{p}(1-0.59\kappa). \tag{41}$$

By substituting (41) and (39) into (40) and by rearranging, then k_e is expressed by

$$k_e = \frac{\pi}{Q}(1-0.59\kappa). \tag{42}$$

With κ fixed previously, it follows from (42) that k_e is a function of Q or else p, as $p/Q = 4/3$ previously for the best winding layout.

C. Air-Gap Flux Density

In Fig. 16, the air-gap flux density waveforms obtained from the FE analysis are shown for the optimum designed air-cored RFPM generator. The flux density waveforms are at the inner and outer halves of the stator winding. It is clear that the curvature has little effect (1.38% in the peak values) on the difference between these flux density waveforms. This can be explained by the relatively large air-gap diameter and high pole number of the generator, which is always the case in low-speed direct drive wind generators.

The curvature effect of the double-sided PM rotor is more observable in the flux density waveforms at the magnet surfaces, as shown in Fig. 17. Here, the difference in the flux density at the middle of the magnet poles is 6%. This difference will cause the saturation of the inner and outer back iron yokes to

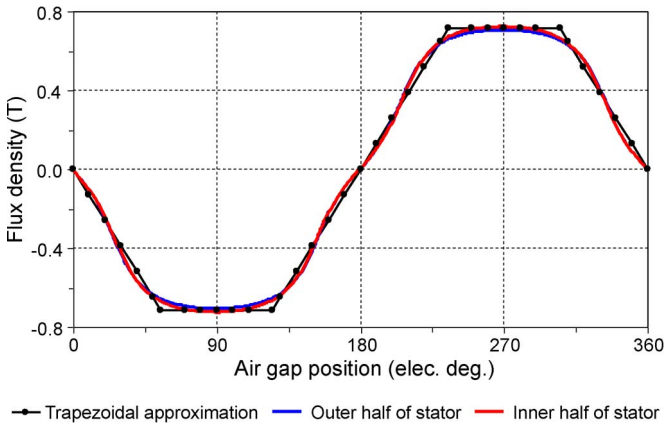

Fig. 16. FE-calculated radial air-gap flux density waveforms at the inner and outer halves of the stator winding.

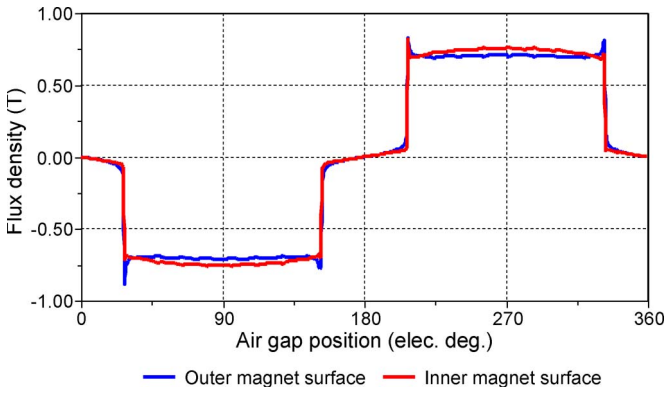

Fig. 17. FE-calculated radial flux density waveforms at the surfaces of the inner and outer PMs.

differ. Inversely, however, the magnetic-circuit lengths of the iron yokes differ so that the difference in MMF drop across the inner and outer iron yokes will be very small. This effect, hence, is ignored in the analytical model. The average magnet surface flux density at the middle of the magnet is determined from Fig. 16 as 0.73 T.

In Fig. 16, a trapezoidal approximation of the air-gap flux density is also shown. This approximation can be used to determine the ratio $b = B_g/B_1$, which is found to be $b \approx 0.92$ for the case in Fig. 16. The accurate b value for the case in Fig. 16 is $b = 0.937$.

From the FE results in Fig. 16, the average value for the peak air flux density of the prototype generator is $B_{g(FE)} = 0.715$ T. This differs by 1.4% from the designed value of 0.725 T using (19)–(21).

D. Leakage Flux Constraints

There is a tangential leakage flux in the air gap of the air-cored RFPM machine, i.e., between adjacent PMs, and from the PM pole edges to the back iron yoke. These leakage flux paths are shown in Fig. 18. The amount of leakage flux depends on the leakage air-gap reluctances, which, in turn, depend on the lengths of the leakage flux paths. In Fig. 18, these flux-leaking path lengths from the pole edges are ℓ_{ipg} between the magnet poles and h_m from the magnet pole edge to the back iron yoke.

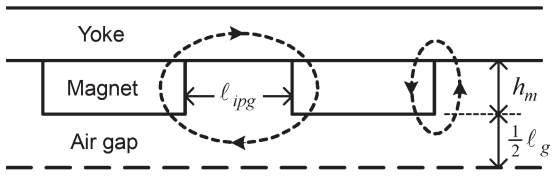

Fig. 18. Leakage flux paths in the air gap of the air-cored RFPM machine.

To prevent flux leaking from the pole edges, the radial air-gap reluctance between opposite magnet poles must be lower than the leakage air-gap reluctances. Hence, the constraints are $\ell_g < \ell_{ipg}$ and $\ell_g < 2h_m$. These constraints are strict, but they ensure that flux does not leak away from the pole edges. Equation (19) can be used to investigate the constraint of $\ell_g < 2h_m$ as follows: take $H_y \approx 0$, $H_c = 923$ kA/m, $B_r = 1.38$ T (from Table I), and $\ell_g = 2h_m$, and then, from (19), $B_g = 0.63$ T. This is an interesting result, which implies that, if B_g is chosen in the design as $B_g > 0.63$ T, then the constraint of $\ell_g < 2h_m$ will never be violated. In the design of the air-cored RFPM wind generator in this paper, B_g is set equal to $B_g = 0.725$ T. Finally, the curvature of the double-sided PM rotor will cause the leakage flux to be more severe at the inner PM rotor. Hence, ℓ_{ipg} of the inner PM rotor must be used in the constraint of $\ell_g < \ell_{ipg}$ as in (27).

REFERENCES

[1] M. J. Kamper, "Comparison of linear permanent magnet machine with overlapping and non-overlapping air-cored stator windings," in *Proc. 4th IET Int. Conf. PEMD*, York, U.K., Apr. 2008, pp. 767–771.

[2] M. J. Kamper, R.-J. Wang, and F. G. Rossouw, "Analysis and performance of axial flux permanent-magnet machine with air-cored non-overlapping concentrated stator windings," *IEEE Trans. Ind. Appl.*, vol. 44, no. 5, pp. 1495–1504, Sep./Oct. 2008.

[3] N. F. Lombard and M. J. Kamper, "Analysis and performance of an iron-less stator axial flux PM machine," *IEEE Trans. Energy Convers.*, vol. 14, no. 4, pp. 1051–1056, Dec. 1999.

[4] A. Parviainen, J. Pyrhonen, and P. Kontkanen, "Axial flux permanent magnet generator with concentrated winding for small wind power applications," in *Proc. IEEE Int. Conf. Elect. Mach. Drives*, 2005, pp. 1187–1191.

[5] J. R. Bumby and R. Martin, "Axial-flux permanent-magnet air-cored generator for small-scale wind turbines," *Proc. Inst. Elect. Eng.—Elect. Power Appl.*, vol. 152, no. 5, pp. 1065–1075, Sep. 2005.

[6] R.-J. Wang, M. J. Kamper, K. Van der Westhuizen, and J. Gieras, "Optimal design of a coreless stator axial flux permanent-magnet generator," *IEEE Trans. Magn.*, vol. 41, no. 1, pp. 55–64, Jan. 2005.

[7] G. Tomassi, M. Topor, F. Marignetti, and I. Boldea, "Characterization of an axial-flux machine with non-overlapping windings as a generator," *Electromotion*, vol. 13, no. 1, pp. 73–79, Jan.–Mar. 2006.

[8] E. Rossouw and M. J. Kamper, "Use of air-cored axial flux permanent magnet generator in direct battery charging wind energy systems," in *Proc. 7th Int. Conf. Power Electron. Drive Syst.*, Bangkok, Thailand, Nov. 2007, pp. 1102–1107.

[9] P. J. Randewijk, M. J. Kamper, and R.-J. Wang, "Analysis and performance evaluation of radial flux air-cored permanent magnet machines with concentrated coils," in *Proc. 7th Int. Conf. Power Electron. Drive Syst.*, Bangkok, Thailand, Nov. 2007, pp. 189–195.

[10] A. MacDonald, I. Portugal, M. Mueller, and J. Shek, "A time series approach to design of a permanent magnet synchronous generator for a direct drive wind turbine," in *Proc. ICEM*, Villamoura, Portugal, 2008, pp. 1–6.

[11] S. Drouilhet, E. Muljadi, R. Holz, and V. Gevorgian, "Optimizing small wind turbine performance in battery charging applications," in *Proc. Wind Power*, Washington, DC, Mar. 27–30, 1995.

[12] R.-J. Wang and M. J. Kamper, "Calculation of eddy current loss in axial field PM machine with coreless stator," *IEEE Trans. Energy Convers.*, vol. 19, no. 3, pp. 532–538, Sep. 2004.

[13] DNV/Risø, *Guidelines for Design of Wind Turbines*, 2nd ed. Det Norske Veritas, Copenhagen, Denmark, 2002.
[14] D. N. Mbidi, K. van der Westhuizen, R.-J. Wang, M. J. Kamper, and J. Blom, "Mechanical design considerations of a double-stage axial-flux PM machine," in *Conf. Rec. 35th IEEE IAS Annu. Meeting*, Rome, Italy, 2000, pp. 198–201.
[15] P. P. Benham, R. J. Crawford, and C. G. Armstrong, *Mechanics of Engineering Materials*, 2nd ed. Harlow, U.K.: Pearson Educ. Ltd., 1996.
[16] R. R. Graig, Jr., *Mechanics of Materials*, 2nd ed. New York: Wiley, 2000.
[17] M. J. Kamper, A. J. Rix, D. A. Wills, and R.-J. Wang, "Formulation, finite-element modeling and winding factors of non-overlap winding permanent magnet machines," in *Proc. ICEM*, Vilamoura, Portugal, Sep. 2008, pp. 1–5.

Johannes Abraham Stegmann received the B.Eng. degree in mechatronic engineering from the University of Stellenbosch, Stellenbosch, South Africa, in 2007, where he is currently working toward the M.Sc.Eng. degree in electrical engineering.

His research interests include the use of permanent-magnet (PM) generators in wind turbine applications. His postgraduate studies are on the use of PM air-cored machines in different stand-alone wind energy systems.

Maarten J. Kamper (M'96–SM'08) received the M.Sc.Eng. and Ph.D.Eng. degrees from the University of Stellenbosch, Stellenbosch, South Africa, in 1987 and 1996, respectively.

He has been with the academic staff of the Department of Electrical and Electronic Engineering, University of Stellenbosch, since 1989, where he is currently a Professor of electrical machines and drives. His research interests include computer-aided design and control of reluctance, permanent-magnet, and induction electrical machine drives, with applications in electric transportation and renewable energy.

Dr. Kamper is a South African National Research Foundation Supported Scientist and a Registered Professional Engineer in South Africa.